TGRS-2022-03192

*

Southwestern Australia Acid-Saline Mineralogy: Observations from Reflectance Spectroscopy

Mark Radwin, *Member, GRSS*, Brenda Bowen, Kathleen Benison, and Stacy Story

***Abstract*— Acid-saline sediments in shallow-lake environments in southwestern Australia host complex mineralogical suites representing long-term weathering and modern extreme acid saline chemistry. It is not known whether large-scale reflectance spectroscopy datasets from watersheds across the Yilgarn Craton show regional mineralogical variability. This study assesses over 2,500 spectra from datasets of shallow subsurface sediments by using automatic minima detections for spectral features of interest. Integrating microscopic and spectral observations show that proportionally similar mineral assemblages exist in a variety of recognizable textures. Spectral results indicate iron oxide and phyllosilicates are the most detected mineral types, alongside less common alunite, jarosite, and gypsum. The difference in detection abundance by percentage for mineral groups, particularly iron oxides, accounts for the largest regional variation observed in spectra. Spectral feature characteristics show significant regional variation for iron oxide, alunite, and hydrated mineral absorptions. The spectral observations align with previous mineralogical observations of these landscapes and the expected weathering evolution for granitoids, where Al-phyllosilicates and iron oxides are most prevalent. Observations of these mineral suites enhance understanding of regional differences and similarities in chemical precipitates and products of water-rock interaction in extreme acid-saline environments and have implications for studying sediments and rocks on Mars.**

***Index Terms*— Acid-Saline Sediments, Australia, Iron Oxides, Mars-Analog, Mineralogy, Minima, Reflectance Spectroscopy**

I. INTRODUCTION

THE geology of southwestern Australia presents a rare acid-saline terrestrial environment which contemporarily reflects the consequences of over 60+ m.y. of extreme weathering and water-rock interactions. Some of the landscape is characterized by thick regolith, up to 50+ m in depth, with widely distributed shallow and ephemeral lakes, some with very extreme chemistries. These lakes experience frequent flooding, evapoconcentration, and desiccation cycles and are associated with proximal ephemeral fluvial channels, mudflats, sandflats, and aeolian deposits, in a semi-arid climate [1]–[5]. Previous analyses show that lakes and groundwaters have complex and extreme compositions. Some lake waters are very acidic, with pH measured as low as 1.4, and groundwaters are also typically acidic with an average pH of ~3 [6]–[8]. These waters have been observed with total dissolved solute concentrations up to ~10 times more saline than seawater with water activity as low as 0.717 for the most acidic waters [1], [6], [8]–[10]. However, acidity and salinity of lake and groundwater spatiotemporally vary from mild-to-extreme in response to flooding and evapoconcentration, with no apparent regional chemical gradient, such that multiple samples from an individual lake or samples from proximal lakes may vary significantly both spatially and temporally, due to the impact of localized heterogeneity in composition and surface processes. High concentrations of Fe, Al, Si, S, and other major elements are present in these waters, ultimately providing the necessary constituents for rapid and extensive chemical precipitation as well as alteration of the regolith and bedrock [6], [7]. A wide array of minerals has been observed in the sediments, and the sediments show combined characteristics of argillic ferricretes and sulcretes [11]. In particular, the mineral suite represents long-term supergene weathering and acid-saline precipitation [1], [2], [5], [6], [8], [12], [13]. These observations have also delineated that the sediment mineralogies in the surface and near-surface environments of these lakes are primarily Al-rich-phyllosilicates (mainly kaolinite – $Al_2Si_2O_5(OH)_4$), iron oxide (hematite – Fe_2O_3 and goethite – $FeO(OH)$), halite ($NaCl$), gypsum ($CaSO_4{\cdot}2(H_2O)$), alunite ($KAl_3(SO_4)_2(OH)_6$), jarosite ($KFe_3(SO_4)_2(OH)_6$), and quartz (SiO_2).

The minerals at acid saline lakes form through various processes, including aqueous and eolian deposition in paleochannels, shallow lakes, and associated shorelines and dunes, chemical precipitation from surface waters, weathering of pre-existing rocks, and diagenetic precipitation from groundwaters. Evaporites such as halite and gypsum commonly form as chemical sediments from lake waters, resulting in beds of crystals. Kaolinite, iron oxides, and quartz commonly are weathering products; they are retained in the regolith due to low amounts of mass removal, but are also found as chemical precipitates [14]. Abundant reworking due to sheet floods and winds entrain, transport, and deposit these minerals, including

*This paragraph of the first footnote will contain the date on which you submitted your paper for review, which is populated by IEEE.

This work was support in part by the National Aeronautics and Space Administration through the Solar System Workings program grant 80NSSC19K0552, and by the National Science Foundation grants from the Sedimentary Geology and Paleobiology Program (EAR-0719822, EAR-0719838 and EAR-0719892. Corresponding author: *M. Radwin*

Mark Radwin is with the University of Utah, Salt Lake City, UT 84112 USA (e-mail: markradwin@gmail.com).

Brenda B. Bowen is with the University of Utah, Salt Lake City, UT 84112 USA (e-mail: Brenda.bowen@utah.edu). Kathleen Benison is with West Virginia University, Morgantown, WV 26506 USA (e-mail: kathleen.benison@mail.wvu.edu). Stacy Story was with Purdue University but is now with ExxonMobil, Conroe, Texas 77301 USA (e-mail: stacystory.ss@gmail.com)

Color versions of one or more of the figures in this article are available online at http://ieeexplore.ieee.org

the halite and gypsum. Diagenetic formation of minerals has been documented by multiple studies, finding that all the dominant minerals are formed through various early-diagenetic processes based on interactions with existing regolith, sediments, and local waters [1], [2], [12], [13]. Associated with diagenesis and weathering, very-fine grains, as small as 0.25 micrometers, are prevalent [12]. In contrast to the other dominant minerals, alunite and jarosite are solely diagenetic precipitates, vary regionally, and are diagnostic of acidic, oxidized waters, [15]–[19].

This study explores mineralogical differences of two acid saline lake watersheds in southwestern Australia based on reflectance spectroscopy of regional sediments. We test whether site-based mineralogical characteristics derived from spectra can be linked to regional differences in basement geology and/or surface water geochemistry. Previous studies investigating the mineralogy of southern Western Australia provide major, minor, and trace element data, as well as crystallographic, and reflectance spectroscopic analyses of relatively constrained datasets ($n < 50$) from many study sites, including the areas studied here (Table A1) [1]. [2], [3], [6], [7], [9], [12]. However, the use of reflectance spectroscopy to explore regional mineralogy differences is limited; this work provides insight to how spectral characteristics vary across highly mixed, complex sediments, with focus on the established suite of primarily observed minerals.

Visible-to-short-wave-infrared (VSWIR) reflectance spectroscopy (between 350-2500 nm) provides a powerful, non-destructive method of identifying materials based on the wavelengths of light that are absorbed and reflected. VSWIR reflectance spectroscopy has limitations, especially when used for fine-grained and heterogeneous sediments, such as those in acid-saline lake systems. Intimate mixing of multiple pure or mixed compositional grains/crystals complicates mineralogical identification and the ability to determine proportions of mixed compositions, as does morphological heterogeneity due to coatings or deformation of the grains. Intimate mixing occurs when grain sizes are small enough to allow for a single photon to interact with multiple grains and where internal grain reflections may occur, or where the field-of-view of the spectroradiometer incorporates a swath of photon paths. The result of intimate mixing is non-linear spectral mixing, such that a spectral feature can be shifted, subdued, and/or accentuated. Many of the key minerals in this system show spectral variation for nearly-pure samples and exhibit spectral features similar to one another, such as most phyllosilicates, which can result in broad, shifted or overlapping spectral features when mixed due to the combination of slightly offset overtones [20], [21].

Variability of the spectral character of iron oxides shift due to grain size or mineral phase differences and can be observed in the spectra based on shifts in the absorption wavelength location (minima) and the width and shape of the absorption feature [22]. For continuum-removed spectra (the focus from herein), hematite displays a broad diagnostic crystal field absorption near 900 nm (Figure 1a), while goethite displays a broad crystal field absorption near 960 nm (Figure 1b) [13], [23], [24]. The absorption feature for both hematite and goethite

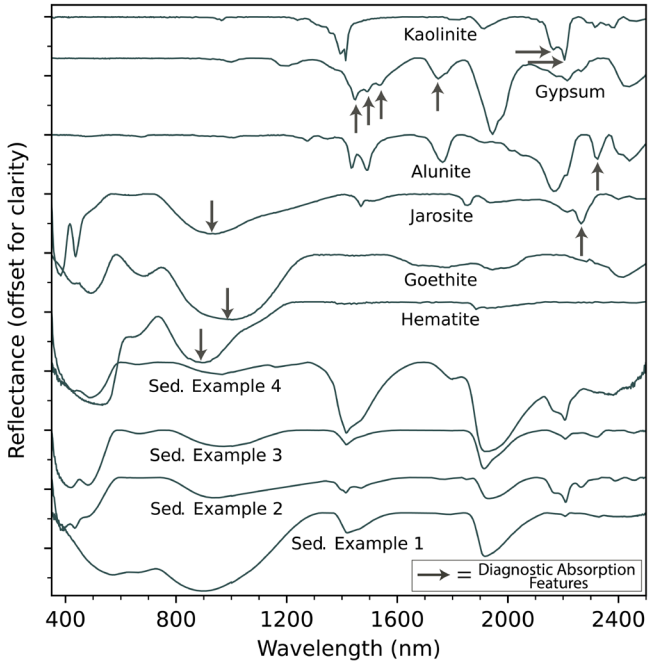

Fig 1. Continuum-removed visible-to-shortwave-infrared (VSWIR) spectra spanning from 350-2500 nm illustrating diagnostic absorption features for pure spectra from the USGS Spectral Library (Clark et al., 2007) as well as three example spectra from sediments assessed in this study. Spectra names, from bottom to top, are sediment example 1 (LA2 690-695 cm), sediment example 2 (WA3_022), sediment example 3 (LA2 3040-3045 cm), sediment example 4 (LB 505-510 cm), hematite (GDS27), goethite (WS222 Crs), jarosite (JR2501), alunite (GDS83), gypsum (SU2202), and kaolinite (CM3 BECKa). Spectra are offset for clarity, where the y-axis tick intervals represent 0.25 reflectance.

shifts from shorter to longer wavelengths, depending upon fine or coarse grain size, respectively [23].

The diagnostic spectral features for phyllosilicates arise from vibrational overtones of O-H and H-O-H (water), where O-H bonds are part of the mineral structure being bound to a metal cation adjacent to octahedral layers and water is typically adsorbed to the crystal surface or trapped in an interlayer. For pure phyllosilicates, individual or combined overtone O-H vibrations are located as absorptions near 1400 nm (O-H stretch overtone) and between 2200-2500 nm (metal-O-H bends and combinations), while absorptions due to H-O-H vibrational overtones are located near 1410 nm and 1920 nm [20], [21], [25]. O-H and H-O-H absorption features both occur near ~1400 nm. Pure kaolinite spectra contain an Al-O-H doublet absorption feature near 2166 and 2211 nm (Figure 1f).

Gypsum has H-O-H and O-H spectral absorption features located at ~1410, 1750, 1950, and 2200 nm (Figure 1e). A sample with a significant amounts of gypsum will show a diagnostic triplet feature near 1400 nm, composed of three absorptions near 1410, 1430, and 1510 nm [21], [23]. However, when the gypsum is in a mixed sample, the triplet signal is commonly subdued, and the feature appears to be broad with an

absorption center located near 1410 nm. The absorption feature near 1750 nm is a strong, diagnostic feature, unlike the absorptions near 1400, 1900 and 2200 nm which can be confused with other mineral absorptions.

Jarosite and alunite are typically early diagenetic precipitates in these sediments, forming intergranular cements commonly accompanied by iron oxides. Jarosite, containing iron and hydroxyl complexes, displays a crystal field iron absorption feature near 940 nm, between the wavelength locations for the diagnostic hematite and goethite absorptions, as well as a diagnostic Fe-O-H absorption feature near 2264 nm (Figure 1c) [21], [23]. Alunite spectra contain Al-O-H absorption features which are shifted from the typical Al-O-H absorption features due to SO_4, seen as a doublet near 1400 nm and distinct absorptions near 1770 and 2170 nm (Figure 1d). Conversely, alunite contains a ~2320 nm OH-stretch absorption which is diagnostic and will be used here for primary alunite identifications as the other alunite absorptions overlap with phyllosilicate and gypsum features. Quartz is not detectable with VSWIR spectra as it is transparent.

This study focuses on three sites with varying basement geology and history of surface processes in southern Western Australia: Lake Aerodrome, Lake Brown, and Twin Lakes (Figure 2). For this research, these three lakes were split between two study regions referred to here as Brown and Norseman, both of which host many other lakes. The two regions are delineated by surrounding watershed or paleodrainage extent, where the Brown region hosts Lake Brown, and the Norseman region hosts Lake Aerodrome and the Twin Lakes. Each basin has unique, but not homogeneous, geochemical boundary conditions based in differences in bedrock geology, weathering history, hydroclimate, and local land use. These sites were once likely hydrologically connected as part of the paleodrainages, however, each site is a modern closed based and there is no known connected surface flow between the sites.

We hypothesized that regional mineralogical variation would be spectrally manifested between these two paleodrainages through shifting of absorption feature minima wavelengths, due to unique spectral mixing characteristics at each site such as grain size distributions, mineral volume percentage ratios, adsorbed species and trace element geochemistry, and the physical extent of mixing.

A large VSWIR spectral dataset from shallow core sediments from Lakes Aerodrome and Brown, consisting of 2,534 spectra in the 350 to 2500 nm range, was produced [26]. In conjunction, a smaller spectral dataset composed of 54 spectra from Twin Lakes was derived from bedrock and surficial sediment samples, as there is negligible regolith at that site. Airborne hyperspectral imagery, collected from Lake Brown and Twin Lakes in 2010, are processed for additional mineralogical context. Microscopy observations from Lake Aerodrome sediments are presented to provide additional information about the nature of these sediments as well as insight into spectral characteristics.

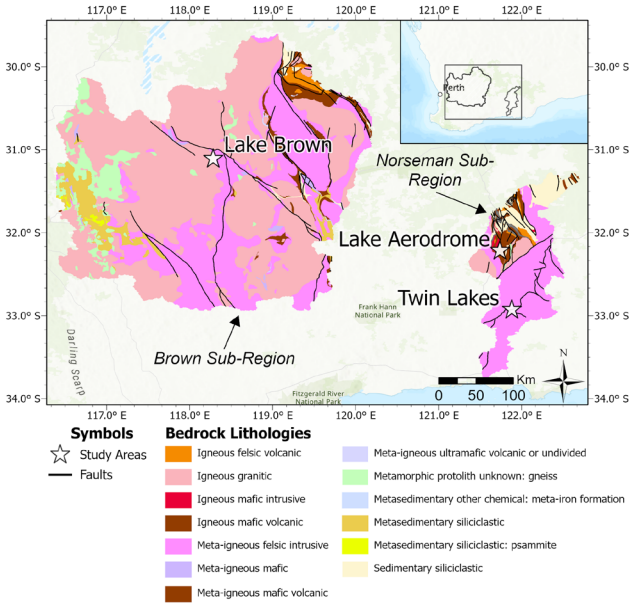

Fig 2. Modified regional 1:100,000 state interpreted generalized bedrock lithology geologic map [27] subset to the two study regions paleodrainage extents, as derived by DEM analysis. Inset map in upper right to orient location in southwest Australia. Scale masks localized observations of various bedrock outcrops at each site.

II. Methods

A. Samples and Datasets

Spectra was collected at 5 cm intervals through four sediment cores from Lake Brown and Lake Aerodrome, creating a dataset with 2,534 spectra (see *Appendix*). These sediment cores were collected in 2009 (Figure 3) [9], and have a maximum depth of ~50 m. There are two core datasets from both sites: LA1 (Lake Aerodrome 1, n = number of spectra =425)), LA2 (n = 1186), LB1 (Lake Brown 1, n = 465), and LB2 (n = 457). Cores were drilled by Boart Longyear using microsonic, dry drilling techniques so drilling would not alter mineralogy and stratigraphy would be preserved. Ten-cm diameter cores were collected in Lexan clear plastic core liners. Drilling was funded by an NSF grant to K. Benison, B. Bowen, and F.E. Oboh-Ikuenobe, with partnership from the Geological Survey of Western Australia and permission granted by Western Australia's Department of Environment and Conservation. The cores were archived at the Kalgoorlie office of the Geological Survey of Western Australia, and representative samples are stored at West Virginia University and the University of Utah.

Samples were analyzed with an Analytical Spectral Device (ASD) FieldSpec 3 spectroradiometer at Purdue University (cores) and University of Utah (surficial sediments). At each 5 cm interval, core sediment was pulverized, then spectrally analyzed with a contact probe to control lighting conditions and minimize atmospheric path length. For all ASD analysis, the spectroradiometer was calibrated at regular intervals (5-20 minutes) using a Spectralon white reference panel.

Airborne-based hyperspectral HyMap [28] datasets for Lake Brown and Twin Lakes were collected by HyVista in collaboration with B. Bowen and K. Benison in 2010. Multiple

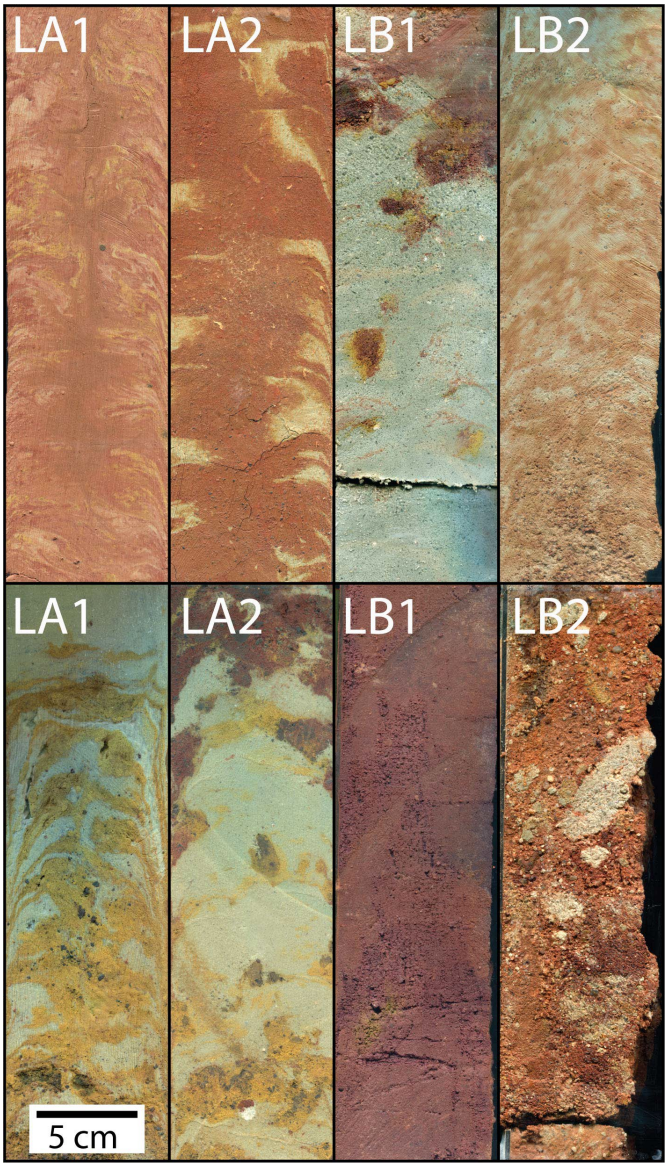

Fig 3. Photographs of representative core slabs from Lake Aerodrome (LA1, LA2) and Lake Brown (LB1, and LB2).

flight lines were stitched together to encompass the Lake Brown area and a single flight line covered the Twin Lakes area.

B. Spectral Processing Methods

Laboratory spectra acquired with the ASD are splice corrected and saved as reflectance spectra prior to processing, although many spectra show a minor splice-error post correction. For spectra to be as comparable and consistent as possible, continuum removal is applied to all spectra across all wavelengths to remove the convex hull (extrapolated local maximum) using ENVI 5.6 (L3Harris). Continuum removal can cause the shifting of spectral features up to 50 nm (seen in this study) where the slope of the convex hull is steep. Therefore continuum-removed spectra cannot be used for direct comparisons with regular spectra. Continuum-removed spectra were processed with functions written in Python to automatically detect absorption features for all spectra, where limits to the width, prominence, and distance between features are implemented to avoid detecting noise or unwanted features.

Automatic detection of spectral features is important for this study to take advantage of the thousands of acquired spectra and avoid the tedious task of manual absorption feature detection. The Python functions used for the automatic detection of spectral features are published by the authors as a package, called RSAbs (Reflectance Spectroscopy Absorptions) and are available online (see *Appendix*). Lower and upper wavelength limits (absorption band short and long absorption band shoulder wavelengths) were defined for the detection of each absorption; the limits used are: 2175 to 2225 for Al-OH, 1400 to 1430 nm for lower H-O-H, 1875 to 1925 nm for upper H-O-H, 1745 to 1760 nm for gypsum, 2315 to 2325 for alunite, and 2260 to 2270 nm for jarosite.

The datasets of absorption feature central wavelengths were processed to histograms as well as Kernel Density Estimate (KDE) probability density functions, which act as smoothed and extrapolated histograms, to assess absorption distributions [29]–[31]. KDE assessments differ from histograms in that they non-parametrically estimate the probability density function of a random variable, based on a set bandwidth, and the continuous extrapolation of probability density provides details regarding how minima would be distributed with a larger population. Histogram bin widths were set to 10 nm, while the KDE factor used to control KDE bandwidths range from 0.001-0.5 depending on the spectral range for each feature.

In addition to automatic absorption feature detection algorithms, polynomial fitting was applied to spectra between 820 to 1200 nm to eliminate effects of noise and smaller overprinted absorptions which degrade the ability to accurately delineate the minima of iron crystal field absorptions. Polynomial fitting was also performed utilizing author written code in Python *(see Appendix)*, where a fourth-degree polynomial equation is calculated for each spectrum, given the wavelength limits, and the local minima is calculated from each polynomial equation. The resulting lists of local minima were filtered between 860 to 990 nm, as those are the estimated limits of minima for iron crystal field absorptions and removes invalid results. Additionally, R^2 and standard error were calculated for each fitted spectrum.

The hyperspectral aerial HyMap datasets *(see Appendix)* were atmospherically corrected by HyVista Corporation using a proprietary radiative transfer methodology, have a pixel size (ground sample distance) of 5 m, and spectral resolution of 15 nm over 128 bands from 450-2500 nm. Atmospheric effects in the imagery are strong and prevent utilization of bands between 1240-1500 and 1740-2040 nm for ground surface analysis, limiting the number of usable bands to ~100. From the limited number of usable bands, the HyMap spectra don't clearly display shoulders and minima of absorption features, which is compounded by significant amounts of noise, thus classification maps prove more useful than direct investigation of the spectra. Processing of the hyperspectral imagery was performed in ENVI 5.6 where supervised spectral angle mapper (SAM) classification images were produced using manually trained classes (included in *Appendix*) and a maximum spectral angle threshold of 0.18 for Lake Brown and 0.2 for Twin Lakes. The spectra of pixels throughout each scene were reviewed to have a general understanding of which regions reflect very

general spectral and land-cover classes. Training data for bright halite crust, dark halite crust, phyllosilicates-or-gypsum, iron rich sediments, iron rich soil under light grassy vegetation cover, dense vegetation, and grassy vegetation classes were manually selected as multiple regions of interest throughout the scene(s). Given the spectral resolution and noise of the HyMap data, the classification map results are to be assessed as general representations of surface distribution rather than precise representations. However, SAM rule images (included in *Appendix*) indicate most classified pixels have spectral angles significantly less than the maximum spectral angle threshold. Although no field measurements of mineralogy were collected to provide an exact ground-truth reference of these data, multiple lines of analyses by the team through the years evaluating the composition and spatial distribution of the sediment mineralogy in these landscapes support the training class choices and spectral interpretations presented here.

III. Results

A. Absorption Minima Detection and Polynomial Fitting Performance and Errors

Although the accuracy of automatic absorption detection algorithms will vary depending on the spectral resolution of the data and characteristics of the absorptions of interest (symmetry, depth, etc.), an assessment of the algorithm's performance on 100 randomly selected spectra from this study indicate the algorithms are very reliable for investigating variability of absorption minima. From the 100 randomly selected spectra, 235 detected absorption minima are compared to the manually determined minima which correlate with an R^2 of 0.99 and average minima-wavelength difference of 0.31 nm. These results indicate the automatic minima detection accurately determines the minima wavelength with only one false-positive detection out of 235. However, the automatic detection does appear to miss on detecting some broad or weak H-O-H, gypsum, and alunite absorptions, resulting in the percent of absorptions detected to be roughly 85% and a max false-negative frequency of 15%. This suggests the automatic detection works moderately well at detecting absorptions for which minima needs to be determined, but also that some error must be considered when assessing or comparing the quantity of detected absorptions. These pitfalls may be addressed by changing the detection sensitivity for specific wavelength ranges.

Separately, our initial assessment of the 2,588 spectra shows that for a vast majority of spectra with a diagnostic ~900-950 nm iron oxide crystal field absorption there is a small but significant absorption overprinted on the broad crystal field feature at ~965 nm. To avoid this or other overprinted features from being detected as the minima location for iron crystal field absorptions, fourth-degree polynomial fitting is applied and used for calculation of the minima wavelength between 820 and 1200 nm. The results of polynomial fitting show an excellent fit (Figure 4), with an average R^2 of 0.924 and successful removal of any overprinted absorptions while retaining the overall shape and minima location of the crystal field feature. The high R^2 provides significant confidence in the calculated minima wavelength for each spectrum. Unlike the absorption detection method, all minima between 820 and 1200 nm should be accounted for and initial assessments observed no false-positive minima calculations.

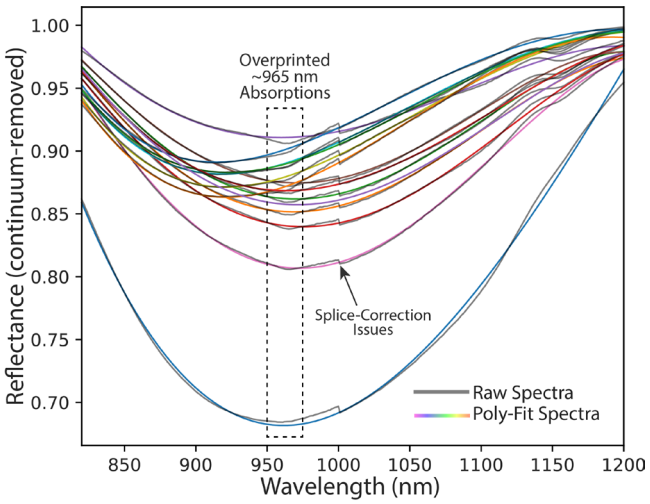

Fig 4. Example polynomial fit spectra alongside the continuum removed spectra, demonstrating the quality of fit, various iron minima locations, and overprinted features

B. Spectral Minima Distributions

The subsequently calculated minima wavelength for all iron crystal field absorption showed differing distributions for each core dataset, where two of the cores display a bimodal distribution and the other two a broad or skewed distribution (Figure 5 a-d). The two datasets with bimodal distributions are LA2 and LB1, where the lower wavelength distributions have an average of ~914 and ~891 nm, respectively. Likewise, the upper wavelength distributions have an average wavelength of ~970 and ~945 nm for LA2 and LB1, respectively. The unimodal datasets of LA1 and LB2 have average wavelengths of ~918 and ~926 nm, respectively. Results from the Twin Lakes surficial sample spectra show a unimodal distribution skewed to larger wavelengths, with an average wavelength of 932 nm.

The absorption detection results illustrate similar absorption distributions among the study regions for commonly detected H-O-H and Al-OH absorptions (Figure 5 e-h). Between these two types of features, the H-O-H absorptions exhibit the greatest amount of wavelength variability for minima, where the ~1900 nm H-O-H feature distributions have an average range of ~32 nm and minima of 1931 nm. In contrast, the Al-OH absorption distributions have an average range of ~10 nm, with the lowest range for a dataset being only ~2 nm, and minima of 2207 nm. Considering the spectral resolution of the ASD spectrometer, these small spectral differences may be insignificant. Twin Lakes samples show similar distributions, with an average minima wavelength of 1920 nm for upper H-O-H absorptions and 2209 nm for Al-OH absorptions.

The number of absorptions detected as features associated with gypsum, alunite, and jarosite for the study sites is less than half of that for either iron oxides or phyllosilicates. The average wavelength associated with the diagnostic gypsum absorption is 1750, 1752, 1750, 1750, and 1755, for the LA1, LA2, LB1, LB2, and Twin Lakes datasets, respectively. The average range

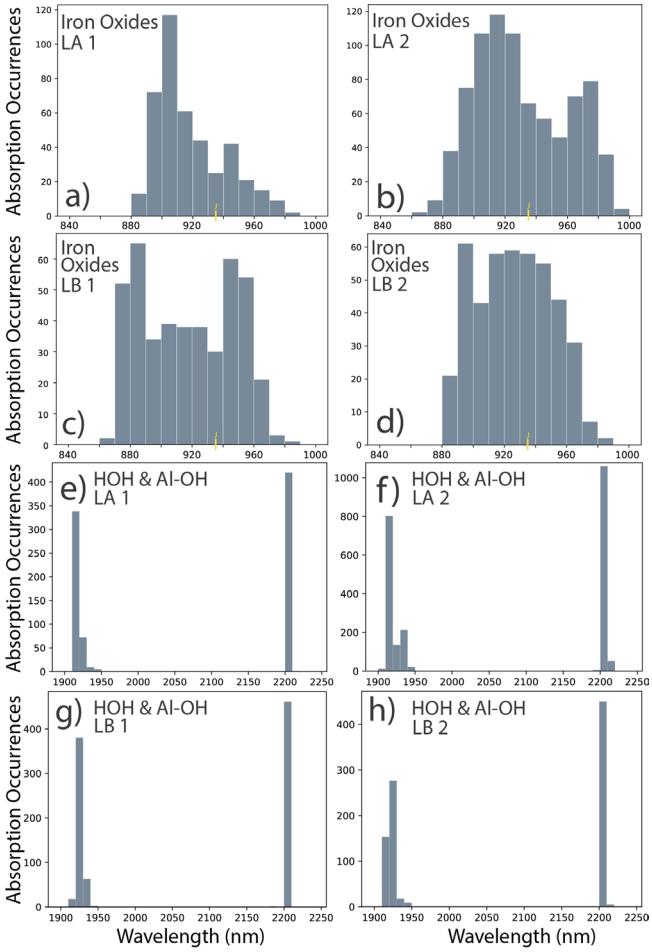

Fig 5. ASD FieldSpec-derived spectral absorption wavelength-center distributions showing absorption detections versus wavelength with bin sizes of 10 nm for iron oxide features from Lake Aerodrome (a-b) and Lake Brown (c-d), and H-O-H and Al-OH features from Lake Aerodrome (e-f) and Lake Brown (g-h). Yellow line at 935 nm (a-d) indicates average wavelength of jarosite for sediments observed in this study.

in wavelength of the gypsum feature is ~9 nm, indicating the features minima is consistent between the study regions. Alunite detections have an average wavelength of 2319 for both LA datasets and 2320 nm for both LB datasets, where the range of detections span from 2315 to 2325, the limits set for detection, for each dataset. Twin Lakes alunite detections show an average wavelength of 2318 nm and range of 9 nm.

Detections of jarosite are limited, with only 22 detections in the LA2 dataset and one detection in the LB2 dataset. However, of the 54 Twin Lakes samples, there are 20 jarosite detections. The average wavelength of the jarosite absorption in the LA2 dataset is 2267 nm, the single absorption in the LB2 dataset has a wavelength of 2263 nm, and the average of in the Twin Lakes dataset is 2266 nm. For all the spectra containing a diagnostic jarosite absorption, the corresponding iron crystal field absorptions have an average minima wavelength of 935 nm and a range of ~70 nm.

C. Surficial Meter-Scale Hyperspectral Imagery

I. Brown Region Classification Map

Our classification image results for the Lake Brown site, representing the Brown region, indicate much of the iron oxide bearing sediments are in a paleochannel system northwest of the main body of Lake Brown (Figure 6a, b). Lake Brown has few iron bearing sediment detections, but there is a thin 5-50 m rim of iron oxides bordering much of the dry lakebed (Figure 6c). During the time of image acquisition, much of the lakebed is dry, such that there is a large salt crust spanning the lake bottom (Figure 6c). Sediments displaying H-O-H and possible metal-OH absorptions are found to be associated with some sections of the paleochannel network to the northwest (Figure 6b) as well as almost all dry lakebeds in the scene (Figure 6a, c, d).

For the dozens of other dry lake beds in this scene that are a part of the Brown region, there is a consistent pattern of iron oxide detections occurring on the borders of lake bodies, even especially small (<~0.05 km2) shallow lake/crustal bodies. A small percentage of the shallow dry lake beds have an identified salt crust. Proximal to the paleochannel system, as well as the shallow dry lake beds, there is dense vegetation. Further from these features are less dense, grassy vegetation, which appear to be part of agricultural land use. Much of the grassy vegetation has sparse coverage with space between the vegetation, which results in mixed signals between the soil underneath and vegetation, leading to a weak but detectable iron oxide feature. Iron rich sediments account for 8%, bright and dark crusts account for a combined 13%, phyllosilicates-or-gypsum account for 13%, dense vegetation accounts for 11%, grassy vegetation accounts for 21%, and iron rich sediments under grassy vegetation accounts for 34% of the mapped area.

II. Norseman Region Classification Map

Our classification image results for the Twin Lakes HyMap imagery in the Norseman region indicates a markedly different landscape (Figure 7), with many more scattered lakes of much smaller size and an absence of obvious associated paleochannel features. To the northeast of Twin Lakes, towards the top of the map, is a large shallow lakebed which predominantly hosts phyllosilicates or gypsum, with 50-600 m wide scattered salt crusts. Iron oxides bound the extent of much of the lakebed (Figure 7b) but are relatively narrow in width. A concentrated zone of pixels with detected iron oxides proximal to or in contact with phyllosilicates or gypsum is present for the area just to the northeast of this large lakebed, associated with smaller lakebeds.

All of the other lakebeds in the scene have salt crusts and a consistent pattern where the bright crust is to the north and the dark crust is to the south of the crustal body (Figure 7c,d). These lakebeds are rimmed with phyllosilicates/gypsum towards the center-outwards then iron oxides near the margins, but some of these beds have oblong phyllosilicates/gypsum and iron rich sediments stretching to the east (Figure 7c). In the aerial image, Twin Lakes is a small lakebed near the bottom of the map (Figure 7d) with a road transecting through. The road transecting Twin Lakes is identified as iron rich sediments, which is consistent with field observations that roads in the region are paved with iron oxide concretions [2]. With regards to percent of area mapped, iron rich sediments

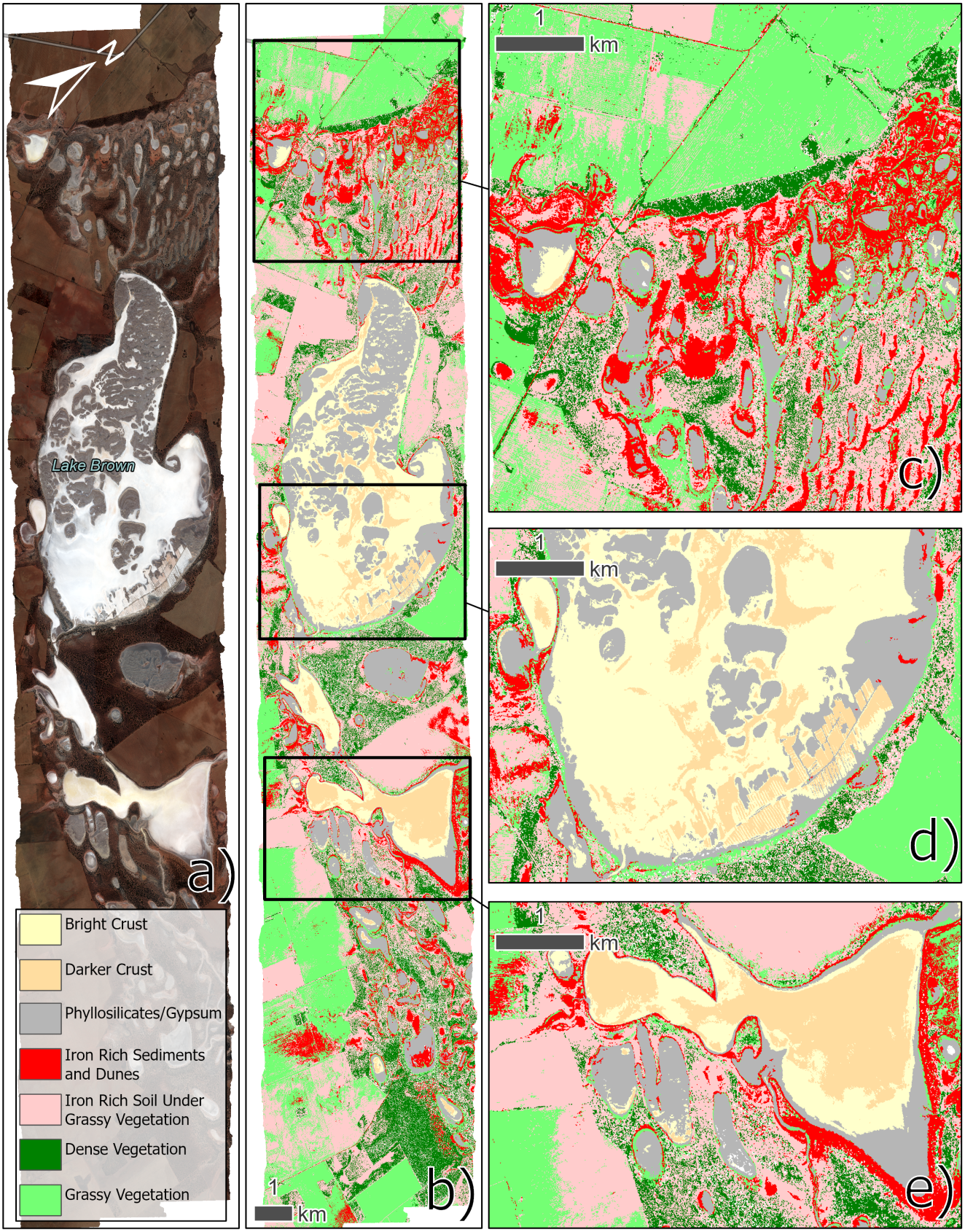

Fig 6. True-color (a) and classification (b) map of Lake Brown and the proximal area, with insets (c-e) to provide extra detail for regions with features of interest. Yellow = bright crust, orange = darker crust, gray = phyllosilicates or gypsum, red = iron rich sediments and dunes, pink = iron rich soil underneath grassy vegetation, dark green = dense vegetation, light green = grassy vegetation. White pixels indicate unclassified pixels that didn't fall within the max spectral angle of 0.18 for any class.

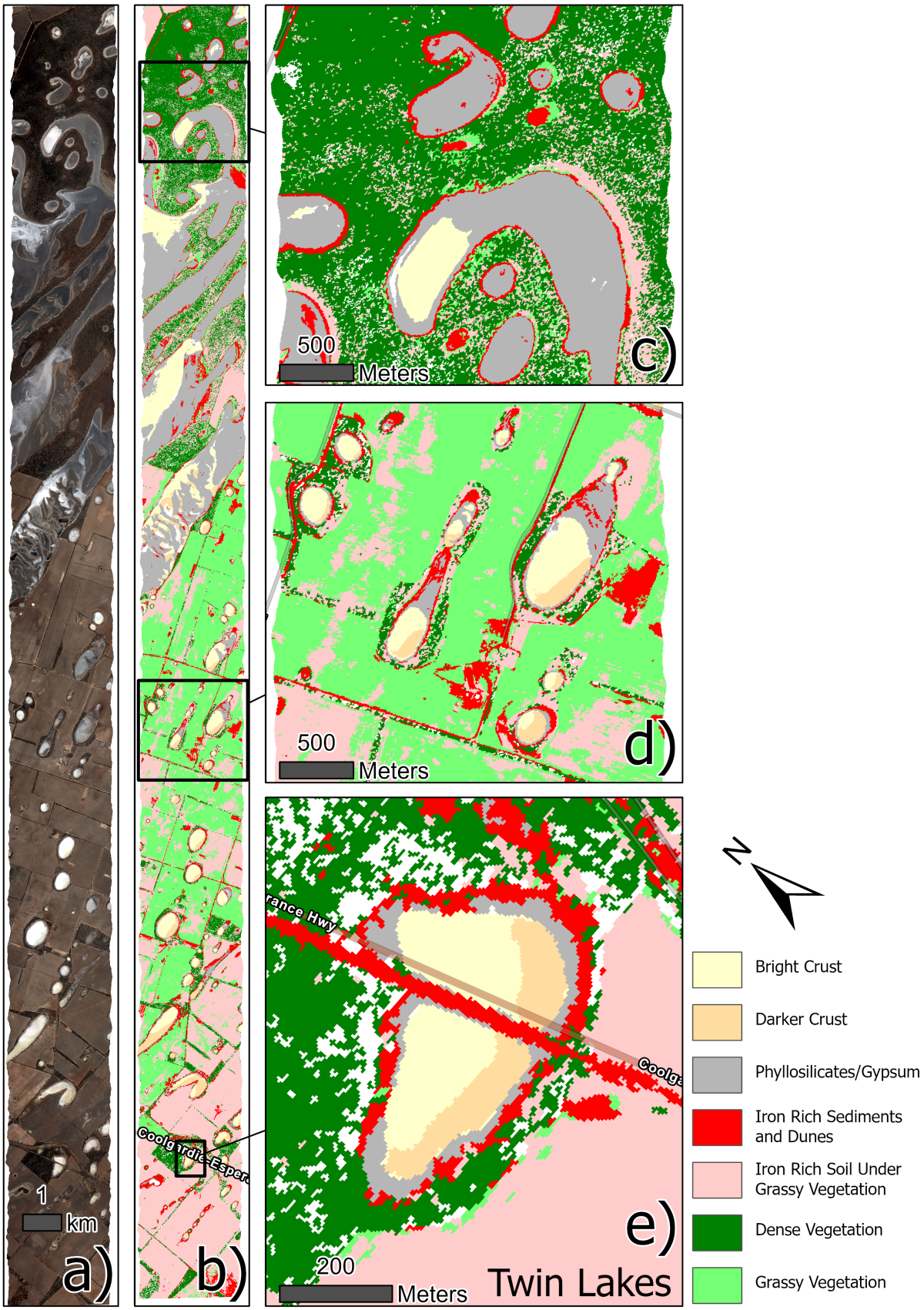

Fig 7. True-color (a) and classification (b) map of Twin Lakes and the proximal area, with insets (c-e) to provide extra detail for regions with features of interest. Yellow = bright crust, orange = darker crust, gray = phyllosilicates or gypsum, red = iron rich sediments and dunes, pink = iron rich soil underneath grassy vegetation, dark green = dense vegetation, light green = grassy vegetation. White pixels indicate unclassified pixels that didn't fall within the max spectral angle of 0.20 for any class.

account for 6%, bright and dark crusts account for a combined 6%, phyllosilicates-or-gypsum account for 17%, dense vegetation accounts for 15%, grassy vegetation accounts for 24%, and iron rich sediment under grassy vegetation accounts for 31%. Overall, the Lake Brown map has a greater percentage of halite crusts and iron rich sediments while the Twin Lakes map has a greater percentage of phyllosilicates-or-gypsum as well as grassy and dense vegetation classes.

D. Observations from Microscopy Relevant to Spectra

Thin sections from the LA2 core provide a glimpse into the complex nature of these near-surface sediments and help to understand what a spectrometer is observing at mm-cm scale field-of-views. High porosity, estimated between 10-40%, is observed for nearly all the near-surface thin sections, as shown by the blue infilling epoxy (Figure 8). Mineralogical identification using microscopy petrographic techniques is challenging in these sediments given high levels of physical mixing and extremely small grains, but allows for general assessment of composition and texture. Iron oxide cementation in radial formation patterns is common within the phyllosilicate matrix which form in close proximity and assemble as bands or unorganized zones in larger field-of-views (Figure 8a-b, f). The most porous zones are associated with unconsolidated sub-angular to sub-rounded grains of gypsum and quartz with patchy intergranular iron oxide cementation (Figure 8b, e-f). Tan colored, extremely fine-grained sediment interpreted as phyllosilicates are widely observed throughout thin sections that mainly form in cohesive packets encompassing much of the thin section.

Dense iron oxide cementation appears to be most associated with unconsolidated grains. Additionally, it is common to find small radial patches of iron oxide superimposed on gypsum grains (Figure 8d) and as delineating gypsum growth bands (Figure 8c). Given the high amounts of SiO_2 reported in previous studies, an abundance of quartz is expected, however, quartz grains are challenging to identify in thin section, suggesting the quartz may be very fine grained, coated by iron oxides, or amorphous opal.

Our observations illustrate that, in reference to an ASD spectrometer with a ~cm-scale field-of-view, the spectral signals are the result of light interacting with the same mineralogies but in differing physical mixing conditions. Ultimately, this leads to spectra with common characteristics due to the additive nature of spectra. High porosity, and the association of porosity with iron oxide coatings, suggests iron oxides are likely detected by the spectrometer even if the sample appears to lack visible iron. Similarly, high porosity allows for multiple internal reflections which amplifies spectral mixing. Given the small size of grains, precipitates, and mineralogical zones in many of the thin sections, it is also likely that the individual fiber optic strands, separating the spectrometer FOV, may be viewing different mineralogies.

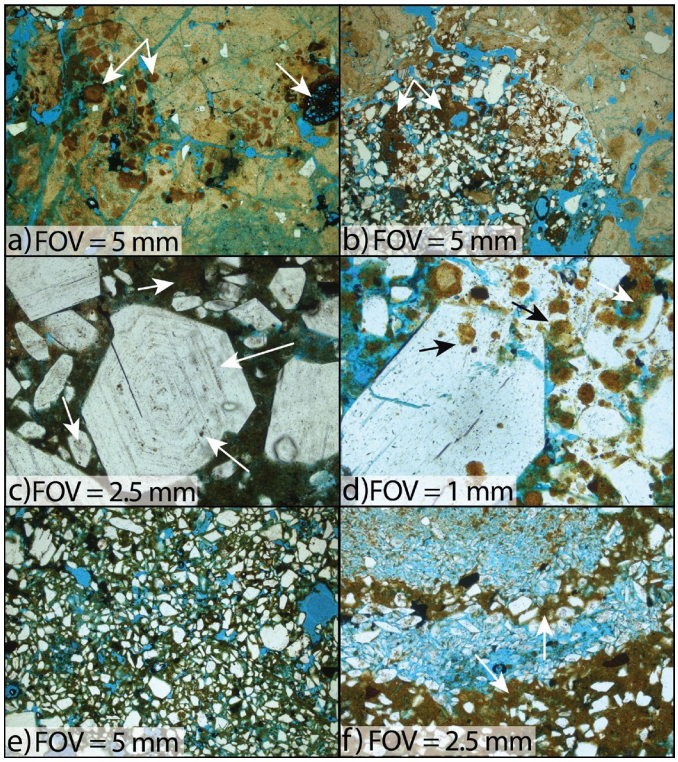

Fig 8. Petrographic microscopy images of thin sections from the LA2 (Lake Aerodrome) dataset, illustrating a) globular iron oxides, patchy phyllosilicates, and possible rozenite (globular structure in upper right), b) intergranular iron oxide growth with gypsum and quartz grains as well as surrounding phyllosilicates, c) gypsum grains with growth bands including iron oxides and surrounded by intergranular iron oxides, d) gypsum and quartz grains with radial iron oxides growing between and on grains, e) unconsolidated gypsum and quartz grains with intergranular iron oxide growth, f) unconsolidated gypsum and quartz grains with dense bands of intergranular iron oxide growth. Redder iron oxides are more associated with hematite, while greener iron oxides are more associated with goethite. Blue infilling is epoxy, representing pore space.

IV. Discussion

A. Detection Frequency Distribution of Minerals

Associating spectral observations to relative abundances (recurrence based, not volumetric) of major mineral groups found between study sites is potentially a valuable tool to assess mineralogical distributions and provide a spectral bulk analysis which may be compared to appropriate quantitative chemical analyses. To accomplish this, the percentage of spectra from each dataset with detections for a specific mineral is assessed. It is assumed, given the large number of spectra per dataset ($n > 500$), that the combination of the two datasets from Lake Aerodrome and Lake Brown provide a representative comparison of observed spectral features for each location and is a sufficient method to probe regional relative mineral abundance distribution based on the detection frequency. Data from Twin Lakes are also included, although the dataset is much smaller, represents only surficial sediments and rocks, and is likely influenced by sample bias, but still provide a reference to compare to the large sample datasets. The assessment provides a contrasting comparison between the study regions and highlights dominantly detected minerals throughout all the sediments (Figure 9).

Based on the comparisons, the greatest mineralogical differences amongst these three sites are associated with

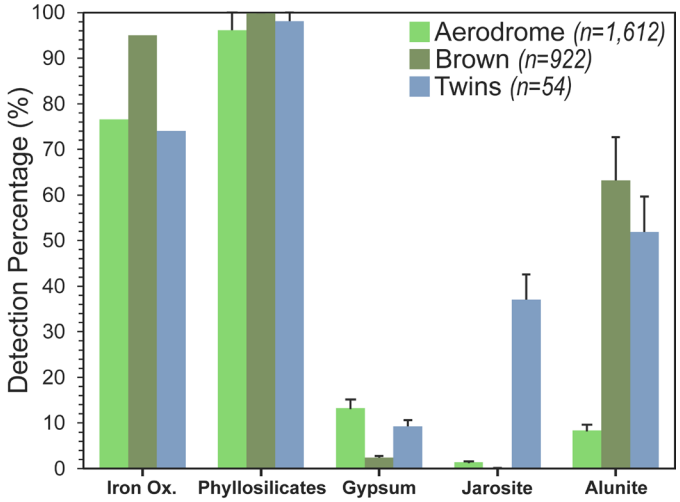

Fig 9. Detection frequency (percentage) of subsurface sediment spectra with mineral species detections per study area (n = number of total spectra). Bright green (left bars) are Lake Aerodrome, dark green are Lake Brown (center bars), and light blue (right bars) are Twin Lakes. Error bars indicate possible range of overlap (15%) associated with the initially reported frequency of false-negative (missed) absorptions when using the automatic detection method. No error bars are shown for iron oxide detections as all spectra were deliberately assessed for iron oxides based on polynomial fitting.

sulfates and iron oxides. Phyllosilicates are widely detected and show the greatest consistency of abundance percentage, which is expected given the ubiquitous nature of phyllosilicates among these highly weathered sediments. Of all the spectra, 98% contain detected phyllosilicates. Iron oxides are the second most widely detected mineral species, but there are significant differences between detection percentages for spectra from the Brown region compared to the Norseman region. Detection percentages for iron oxides at Lake Brown are approximately 95%, nearly 20% greater than at Lake Aerodrome or Twin Lakes. Although detection percentages for gypsum are low for all the datasets, Lake Brown detections appear to be significantly lower at ~3% than the ~8-12% at the Norseman sites. Jarosite detections are extremely rare in the Lake Brown sediments, while it is detected in minor amounts within the Lake Aerodrome sediments and in great amounts for the surficial Twin Lakes samples. Alunite appears to be the third most common mineral and is detected in more than 50% Lake Brown and Twin Lakes spectra, but only 8% of Lake Aerodrome spectra. Conflicting differences between regionality for alunite detections suggests Twin Lakes may share some greater similarities with Lake Brown.

Overall, the detection frequency results illustrate there are greater potential differences between the study areas than initially expected, given each site shows a unique distribution of detection frequencies. These differences indicate that although these sediments illustrate similar regional processes, the geochemical conditions at each site must be significantly influenced by other factors besides regional fluid composition and redox reaction-front oscillations. Additionally, these results dissuade the hypothesis that Lake Aerodrome and Twin Lakes sediments should share more similarities in comparison to Lake Brown sediments. However, the smaller, surficial dataset from Twin Lakes shows comparable detection percentages for iron oxides, phyllosilicates, and gypsum compared to the Lake Aerodrome, which suggests smaller spectral datasets may provide similar interpretations compared to larger, more comprehensive spectral datasets.

The detection results for Lake Aerodrome compare well to LA2 subsample XRD results (Table A2), which indicate that the most-to-least abundant minerals are kaolinite, gypsum, iron oxides, alunite, and jarosite. This agrees with the detection frequency results, except that XRD indicates gypsum is more prevalent than is suggested from spectral interpretations. Similarly, comparing detection frequency results to Lake Aerodrome and Twin Lakes subsample pXRF results (Tables A3 and A4) show agreement, in that greater abundances of pXRF detected Al and S are associated with Twin Lakes samples, which show a greater percentage of alunite and jarosite absorptions. These comparisons help provide more confidence in the spectral interpretations. However, in general it is difficult to compare volumetric compositional analyses, such as XRD, to surficial compositional analyses, such as reflectance spectroscopy.

B. Interpretations from Minima Distributions

From Kernel Density Estimate (KDE) distributions of ASD data, more detailed comparisons can be assessed for each diagnostic mineral absorption feature. KDE distributions for iron oxide crystal field absorptions highlights the separation between unimodal and bimodal distributions between these datasets as well as the complexity of variability (Figure 10a).

Although the distributions from both Lake Aerodrome represent sediments from the same study area, the LA1 iron oxides are densely concentrated around ~910 nm while the LA2 iron oxides are offset ~5 nm higher and exhibit a pronounced shoulder from a lesser occurring distribution of absorptions near 960 nm. The LA2 iron oxides extend into the longer wavelengths more than any of the other datasets. Lake Brown KDE distributions show even greater differences, where the LB1 iron oxides show a stronger bimodal distribution with different average wavelength locations than the other datasets. Additionally, the LB2 iron oxides distribution appears more like the LA2 distribution than compared to the LB1 distribution.

Provided that jarosite detections are minimal, and jarosite contributes to absorptions near ~930 nm, the existing continuum of absorption minima between ~900 to ~960 nm must indicate either grain size variations of hematite or goethite, mixing of hematite and goethite, or a combination of grain size variation and mixing. Overall, the spectral results indicate the predominant form of iron oxides in these sediments is hematite rather than goethite. The cause for a dominance of hematite is unknown, but it is likely inherently related to aqueous conditions of formation, such as pH, temperature, concentrations of Al, and other complex factors controlling iron oxide speciation or transformation [32]. Alternatively, recycling of iron oxide sediments on the surface by wind may be partly responsible. It is likely paleochannel deposits near Lake Brown and similar sites are rich in iron-rich sediments resulting from physical reworking.

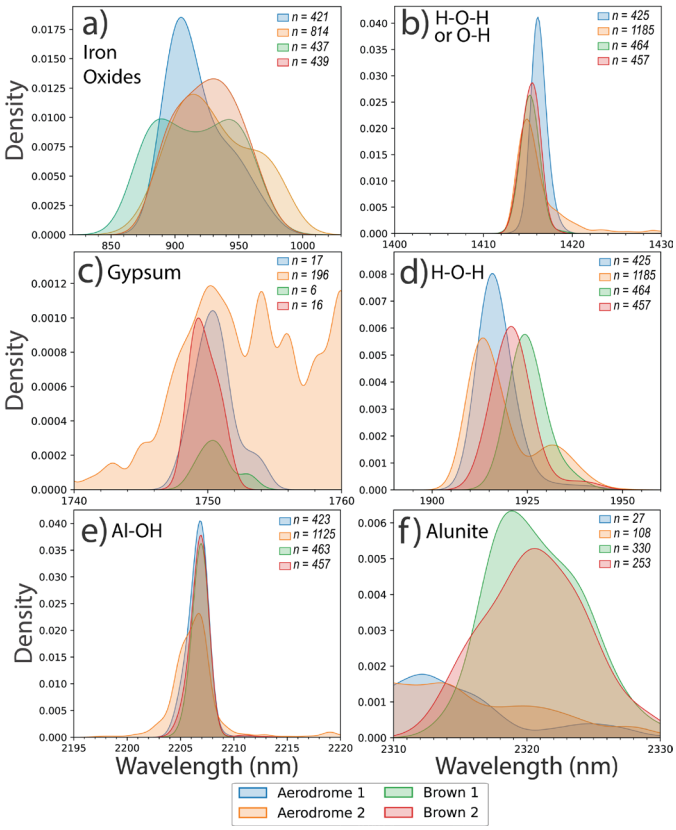

Fig 10. Subsurface sediment ASD spectra derived kernel density estimate (KDE) derived probability density functions of a) iron oxide absorption feature wavelength distributions (K_f of 0.5), b) lower-SWIR H-O-H or O-H (~1400 nm) absorption feature wavelength distributions (K_f of 0.005), c) diagnostic ~1750 nm gypsum absorption feature wavelength distributions (K_f of 0.001), d) upper-SWIR (~1900 nm) H-O-H absorption feature wavelength distributions (K_f of 0.005), e) Al-OH absorption feature wavelength distributions (K_f of 0.001), f) diagnostic ~2320 nm alunite absorption feature wavelength distributions (K_f of 0.005). K_f represents the author-set KDE factor (kde.factor) used by the SciPy.stats Python package [29] to scale the covariance matrix and control bandwidth size. Included in each panel is the number of detected absorptions for each dataset, denoted by "n = #".

The distribution for LA1 is interpreted to indicate a predominantly hematite-rich population with low amounts of grain size variation given the relatively constrained range and average wavelength of ~905 nm. In contrast, the bimodal distribution and shift to higher wavelengths for the LA2 dataset is interpreted as a combination of minor amounts of grain size variation (to coarser grain size) and mixing of hematite and goethite. The LB1 dataset is similar, but with a greater extent of grain size variation, possibly to finer grain size, causing the bimodal distribution to be shifted ~25 nm lower than the LA2 distributions. For both the LA2 and LB1 datasets, the distance between the average wavelength of the hematite and goethite populations are separated by ~50 nm, likely reflecting grain size characteristics. The hematite and goethite grains are likely of similar size for each individual dataset, given the distance of ~50 nm is the nearly the same between the datasets.

Spectral features typically associated with phyllosilicates show the variability of Al-OH absorptions minima wavelength is minimal and unlikely to capture environmental variability between sites. Significant variation up to ~20 nm is observed for the H-O-H absorptions, particularly the ~1900 nm H-O-H absorption (Figure 10b,d), while minimal variation in wavelength position is observed between sites for the Al-OH absorption near ~2207 nm (Figure 10e). The most significant variations for the Al-OH absorption are associated with well-defined Al-OH doublets in the LA2 dataset, as seen by the lower wavelength shoulder in the LA2 probability density function possibly attributed to montmorillonite or alunite (Figure 10e). It may be possible for the ~1970 nm alunite absorption to be shifted into the range of these Al-OH absorptions but there appear to be no other populations of absorptions between 2195 and 2220 nm.

For gypsum detections, the 1750 nm absorption feature is a reliable feature in these sediments, in that the feature shows strong consistency between study areas and little variation among the datasets. All datasets share an average absorption wavelength of 1750 nm (Figure 10c). The range of the feature appears to be relatively constrained, as the LA1, LB1, and LB2 datasets show the feature range 6, 4, and 3 nm, respectively, while the LA2 dataset shows significant variation near 1750 nm. The variation observed for the LA2 dataset is likely attributed to shifted alunite absorptions but may also be due to overtones from minor abundances of other hydrated minerals or false-positive detections as there is moderate noise for some LA2 spectra in this wavelength region that could be falsely identified as a small absorption.

Spectral observations for alunite appear among the most valuable to investigate differences between study regions, as the absorption exhibits significant wavelength variability between datasets and reflects some of the largest regional differences in terms of abundance percentage (Figure 10f). Few alunite detections are present for the Lake Aerodrome datasets, but many are present for the Lake Brown datasets. The average wavelength for the LB1 and LB2 datasets are 2318 and 2321 nm, with ranges of 9 and 6 nm, respectively. There are significantly more absorptions near 2318 nm for the LB1 dataset. The Lake Aerodrome datasets contain some features near 2320 nm but only the LA2 datasets contain detected features with a distribution averaging ~2320 nm, albeit not nearly as many as observed in the Lake Brown datasets. The smaller dataset from Twin Lakes contrasts Lake Aerodrome by containing significant amounts of alunite detections, highlighting regional differences.

Detections for jarosite are minimal for the subsurface datasets, with only 1.4% of Lake Aerodrome and 0.1% of Lake Brown spectra containing the diagnostic 2262 nm absorption, suggesting jarosite also highlights significant geochemical differences between regions.

These comparisons highlight the expected spectral nature of highly weathered sediments and show that although the spectra are manifested by mineralogical mixtures, some features appear more prone to significant variations in minima wavelength while others are not. This suggests investigators should avoid using a single minima wavelength for detection of diagnostic features and should take caution when interpreting the cause of spectral shifts as variability is to be expected.

C. Surficial Mineralogical Distributions

Classification map results for Lake Brown and Twin Lakes provides insight into surficial mineralogical distribution, where the definition of mineralogical zoning appears more structured within the Twin Lakes region compared to the Lake Brown region. However, the classification maps show that the Lake Brown area is much more dominated by iron rich dune fields as well as larger and more cohesive zones of iron rich sediment. The Twin Lakes region appears to have less connectivity between lakebeds, more radial shaped lakebeds, and more significant zoning of mineralogies within each lakebed. Most of the lakebeds show a pattern of darker crust to the south of brighter crust, alongside a rimming pattern of phyllosilicates bounded by iron oxides. Some lakebeds have a teardrop shape, where the tailing end of the lakebeds contain a significant zoning of phyllosilicates to iron oxides in an eastward direction.

Overall, surficial distributions appear more dynamic for the Lake Brown environment, which may indicate this region undergoes more active processes on the surface in comparison to the Twin Lakes region. Most importantly, however, is the recognition of more cohesive zones of iron which may explain the greater abundance of iron detections in spectra from Lake Brown. At Lake Brown the surficial iron is well distributed by the network of iron rich dune fields, associated with paleochannel fill, which may act to concentrate iron and aid in distribution of iron through subsurface sediments when groundwater levels are high and/or when there is meteoric input.

Due to a low signal to noise ratio and limited spectral resolution this study does not incorporate direct assessment of hyperspectral imagery spectra, but future studies should aim to incorporate high-spectral-resolution hyperspectral imagery for assessing absorption features for surficial sediments. Likewise, it would be valuable to compare absorption features between subsurface and surficial sediments.

D. Spectral Links to Regional Bedrock Geology

Given local geochemical links to bedrock weathering history, comparisons of spectroscopic observations from different sites are expected to reflect regional similarities or differences in bedrock lithology, to some extent. Bedrock lithologies in each region influence the modern geochemical characteristics found at sites within the basins, as these are the predominant rocks that have been weathered over long periods to provide the chemical constituents observed in the modern landscape proximal to each study area. As a generalization, based on a regional (1:100,000) scale interpreted bedrock geology map, bedrock lithologies in the Brown region are predominantly igneous granitic or meta-igneous felsic intrusive units, alongside other various small occurrences of mafic and sedimentary units (Figure 2; via Government of Western Australia) [27]. In contrast, bedrock lithologies in the Norseman region are predominantly Precambrian igneous and metamorphic rocks of various compositions, including both mafic and felsic rocks. In summary, the Brown region is heavily dominated by felsic bedrock material with a minor mafic component, while the Norseman region differs in that there is a complex distribution of mafic and felsic rocks.

Local structural features may have some impact on local geochemistry, particularly at the Twin Lakes which are proximal to a large fault. Both regions have multiple fault systems spanning much of the area, typically in either a SE-NW or SW-NE orientation. However, the Norseman region has a complex zone of faulting to the north surrounding the Lake Aerodrome site, resulting in various bedrock lithologies in contact over relatively short spatial scales. The Lake Brown and Twin Lake sites are both proximal to long fault systems, however, Twin Lakes is less than 1 km from the fault system, while Lake Brown is over 10 km from the proximal fault system. Additionally, although Lake Aerodrome is surrounded by proximal faults, the closest fault is ~3 km away.

The Norseman sites share more structural similarities but somewhat opposing bedrock regimes, while the Brown region appears to be controlled by a granitoid bedrock lithology and a less structurally affected landscape. This is observed as Lake Brown is situated on igneous felsic intrusive (granitoid) bedrock contacting meta-igneous felsic intrusive (granitoid) bedrock ~1.5 km away, which is also underlying the Twin Lakes site. In contrast, Lake Aerodrome is situated on igneous mafic volcanic bedrock with a complex distribution of igneous felsic volcanic, sedimentary siliciclastic, metamorphic protolith unknown: gneiss, igneous mafic intrusive, meta-igneous felsic intrusive, igneous granitic, and igneous ultramafic volcanic bedrock units (names based on [26]) all within a 15 km radius.

Although Lake Aerodrome and Twin Lakes share a paleodrainage system, their proximal bedrock lithologies differ significantly as Twin Lakes is underlain by igneous granitoids like Lake Brown but Lake Aerodrome is underlain by mafic volcanics (basaltic), based on the regionally interpreted bedrock lithologies. In contrast to the regional geological map, field observations have noted various bedrock outcrops, such as metabasalt and quartzite, at and near Twin Lakes. However, the regolith thickness is unusually thin at Twin Lakes, such that the surface is mainly hard, consolidated bedrock. This contrasts with the other sites where the regolith is over 20 m deep.

Considering the theoretical weathering evolution of bedrock lithologies under typical neutral pH ranges, granitic materials will weather to produce a local enrichment in Al^{3+} and Fe^{3+} alongside altering to produce large amounts of quartz and kaolinite (or the chemically equivalent halloysite) as well as lesser amounts of iron oxides, particularly goethite from the weathering of biotite [33], [34]. Likewise, basaltic bedrock lithologies under typical natural pH ranges weather to also enrich the weathered rock in Al^{3+} and Fe^{3+}, albeit less Al^{3+} enrichment than weathered granites, and produce many of the same minerals found when weathering granites but with greater amounts of iron oxides [34], [35].

However, under acidic conditions the weathering of basaltic materials is drastically different as the resulting rock contains more Fe and Mg oxides alongside pyroxenes, with a significant loss of major cations to solution and minor production of clays [36]. Thus, from the interpreted local bedrock geology proximal to the three sites, it is assumed there should be more geochemical similarities between Twin Lakes and Lake Brown than between Twin Lakes and Lake Aerodrome. This is because they are both underlain and surrounded by felsic igneous material which would have undergone a similar weathering history. The greater abundance of mafic material underlying and surrounding Lake Aerodrome would suggest the area should have experienced less Al^{3+} enrichment and greater

amounts of iron oxide precipitation compared to the other sites, alongside more extensive amounts of weathering as mafic rocks weather more rapidly than felsic rocks.

These expectations from assessment of bedrock lithologies under normal pH conditions are corroborated by spectral observations associated with Al^{3+} from each site, as a greater percentage of alunite bearing spectra is detected for both Lake Brown and Twin Lakes samples, which can be associated with local Al^{3+} enrichment from granitoid weathering. Although hematite is in general the most predominant iron oxide, the proportion of goethite to hematite absorptions is greater for sediments from the Brown region. Goethite has been found to be a common phase in more Al rich systems, which may explain the abundance ratios between the iron oxides [32]. This suggests that regional weathering pathways likely affect the resulting ratios between hematite and goethite abundance.

We hypothesized that a more mafic landscape would host more iron oxide as a weathering product, however much less iron is detected for Lake Aerodrome than Lake Brown. Additionally, although bedrock geology is similar for Lake Brown and Twin Lakes, the detection percentage for iron from Twin Lakes samples is significantly less than that found at Lake Brown and more representative of what is found at Lake Aerodrome. Given that Lake Brown is the only site in this study associated with an infilled paleochannel (Figure 6c), this may suggest other processes, such as redox cycling and desiccation in the regionally extending paleochannels, have a critical role in driving Fe precipitation and could be responsible for the observed differences. This appears to be supported by the classification map of Lake Brown, which shows iron oxide rich sediments concentrated within the paleochannel sediments. Furthermore, theoretical bedrock lithology weathering pathways don't provide any insight to the strikingly nonexistent regolith at Twin Lakes or the greater percentage of sulfate bearing spectra from Norseman sediments. For example, the jarosite detections are only notably found within the Norseman region, where it appears jarosite is more abundant in the Twin Lakes surficial samples than in Lake Aerodrome sediment cores. Additionally, significantly greater amounts of gypsum are detected in the Norseman region spectra than for the Brown region spectra. In contrast, the prevalence of alunite in the Brown region indicates that sulfates are present in significant amounts but are more associated with aluminum bearing phases, perhaps due to localized iron leaching leading to greater aluminum and sulfate availability when oxidized, or aqueous conditions more favorable to the precipitation of alunite such as lower redox potential (Eh) and/or slightly higher pH.

When referencing regional geology at scales of 1:100,000 there are discrepancies between the bedrock lithology and expected regolith thickness for the Twin Lakes region. From the regional geologic map, the Twin Lakes region shares similar regional bedrock lithology to Lake Brown, which boasts a 20+ m regolith, but field observations from Twin Lakes have noted there is little to negligent regolith. It is possible the absence of a notable regolith in this local region is attributed to physical removal due to aeolian erosion or due to locally fault-induced fluid-flow and sediment transport, as the Twin Lakes sediments show evidence of active diagenetic reaction fronts and water-rock interactions [12], [13]. This highlights the possibility that regional differential weathering in southwestern Australia is significantly variable. Similarly, it is likely the regions underwent differing weathering conditions since the start of long-term weathering, as Australia has transitioned to the subtropics region over the past ~100 million years since splitting from Antarctica at latitudes as low as ~70° S [14], [37]. As Australia transitioned to more tropical latitudes the weathering rate increased with increasing moisture, and there could have been a greater climatic differential between these two regions as the continent transitioned to a more stable tectonic position.

Regional surface expressions have been varying since long-term erosion has begun, and the current drainage basins may not reflect the extent of paleodrainages in the recent geological past. Additionally, groundwater flow, which is primarily independent of drainage boundaries, must have greater importance than connectivity of surface waters in distinct paleodrainages. Likewise, microbial activity has been observed throughout these lakes but their influence on mineralogical precipitation is not well understood [4], [10], [38]. These temporally complex factors must have had a significant influence on how regional sediments evolved to their current mineralogical expressions and account for observed mineralogical differences between sites. Thus, future studies should consider the past weathering regime and hydrology when comparing mineralogical and geochemical differences throughout Western Australia, as well as differences in microbial populations.

The weathering evolution of local bedrock geology appears to have significant control over the Al-bearing mineralogies produced within the thick regolith, however, there must be other important controls to account for differences in iron oxides and sulfates. For example, an alternate explanation for the lesser amounts of iron oxides detected in Lake Aerodrome spectra could be associated with regional fault-induced fluid-flow, with sufficiently acidic and reductive waters to strip iron from the regional sediments. Alternatively, it may be that the paleochannel system associated with Lake Brown sediments encourages more efficient iron cycling and transport, leading to the observed surplus of iron in Lake Brown sediments.

E. Implications for Study of Martian Sediments and Rocks

The unusual sediments from acid-saline lake systems in Western Australia may serve as terrestrial analogs for some sediments and rocks on Mars [38]–[41]. The mineral suite detected in our study, consisting of sulfates, chloride, phyllosilicates, iron oxides, amorphous silica, and a siliciclastic component (Table 1), has been detected in several places on Mars, including at Meridiani Planum (i.e. [42], [43]). Our study found that both textural data and compositional data at different scales are important clues in the interpretation of formation processes. In addition, analyses on Mars have also attempted to resolve textural and compositional sediment and rock characteristics in this manner. Spectroscopic analyses, including reflectance spectroscopy, is commonly used by orbiters for remote observations and by rovers for both remote and proximity science. However, making interpretations from spectral data of martian sediments and rocks can be challenging. This study's documentation of reflectance spectra from fine-grained, mineralogically mixed sediments from a

terrestrial extreme environment provides a comparator for reflectance spectroscopic data from Mars.

V. CONCLUSIONS

The use of reflectance spectroscopy provides another perspective for mineralogy, surface processes, and weathering evolution for the sediments at extremely acid-saline lakes in southern Western Australia. The combination of geochemical and textural observations shows the complexity of this natural, modern setting. In this study, reflectance spectroscopy has enhanced the understanding of regional mineralogical distribution and prompted new inquiries regarding the relationship between weathering evolution and the observed abundance of mineralogies.

APPENDIX

Data repository of reflectance spectra, hyperspectral imagery datasets, SAM training data shapefiles, SAM rule images and processing specifications, classification maps, supplemental XRD data, and supplemental pXRF data: https://doi.org/10.5281/zenodo.7765030

Python package for detecting absorption minima locations: https://github.com/radwinskis/RSAbs

Python functions used for polynomial fitting and absorption minima calculation: https://github.com/radwinskis/Spectra-Polynomial-Fitting

Table A1. Summary of previous studies that have identified alunite, goethite, gypsum, halite, hematite, jarosite, and kaolinite at Lake Aerodrome, Lake Brown, and Twin Lakes. X = identified by previous investigator(s) (followed by references).

	Lake Aerodrome	Lake Brown	Twin Lakes
Alunite	X [12], [13]	X [8], [13]	X [1], [9], [12], [13]
Goethite	X [1], [12], [13]	X [1], [13]	X [1], [12], [13]
Gypsum	X [1], [9], [12], [13]	X [1], [9], [13]	X [1], [12], [13]
Halite	X [1], [12], [13]	X [1], [13]	X [1], [12], [13]
Hematite	X [1], [12], [13]	X [1], [13]	X [1], [12], [13]
Jarosite	X [12], [13]	X [13]	X [1], [9], [12], [13]
Kaolinite	X [1], [12], [13]	X [1], [13]	X [1], [12], [13]

Table A2. Synthesized sum, average, max, and standard deviation of XRD whole-rock weight-percent data for 33 subsamples from the LA2 Lake Aerodrome core dataset, with the minerals of focus highlighted gray. Minerals are sorted from most to least average weight percent (left-to-right). Data from Dr. Stacy Story [26]. See appendix datasets for complete LA2 XRD dataset.

	Kaolinite	Quartz	Halite	Gypsum	Dolomite	Palygorskite	Goethite	Pyrite	K-spar
SUM	1023.5	975.0	371.0	168.0	126.0	81.0	80.0	73.0	63.5
AVG	31.0	29.5	11.2	5.1	3.8	2.5	2.4	2.2	1.9
MAX	76.0	83.0	68.0	78.0	63.0	63.0	12.0	28.0	21.0
σ	22.4	24.0	14.2	13.9	15.0	10.8	3.2	6.5	5.1
	Ca-spar	**Clinochlore**	**Anatase**	**Amphibole**	**Biotite**	**Lepidocrocite**	**Hematite**	**Siderite**	**Amesite**
SUM	60.5	53.0	48.5	31.0	29.5	26.0	22.0	22.0	15.0
AVG	1.8	1.6	1.5	0.9	0.9	0.8	0.7	0.7	0.5
MAX	33.0	31.0	10.0	15.0	15.0	17.0	10.0	22.0	15.0
σ	6.1	6.4	2.3	3.1	3.5	3.3	2.2	3.8	2.6
	Alunite	**Eucryptite**	**Talc**	**Annite**	**Jarosite**	**Periclase**	**Ankerite**	**Ilmenite**	
SUM	10.5	6.0	5.0	4.5	3.0	1.0	1.0	0.5	
AVG	0.3	0.2	0.2	0.1	0.1	0.0	0.0	0.0	
MAX	3.0	2.0	3.5	2.0	3.0	1.0	1.0	0.5	
σ	0.8	0.6	0.6	0.4	0.5	0.2	0.2	0.1	

Table A3. Sum, average, max, and standard deviation of portable X-Ray Fluorescence (pXRF) surficial elemental results (units of uncorrected XRF counts) from 58 subsamples of the Lake Aerodrome cores. The table is sorted from highest-to-lowest average, and elements outside the ten highest average values are not included. Instrument used is the Bruker S1 TITAN using dual method with MudrockAir specifications. See appendix datasets for complete pXRF dataset.

	Cl	Si	Fe	Al	S
SUM	1188.1	239.7	194.3	57.4	51.4
AVG	20.5	4.1	3.4	1.0	0.9
MAX	42.0	16.1	24.1	9.3	12.0
σ	11.0	4.6	5.3	2.0	1.5
	Mg	**Ca**	**K**	**Ti**	**Ba**
SUM	32.7	28.3	10.8	4.3	0.8
AVG	0.6	0.5	0.2	0.1	0.0
MAX	3.1	5.9	1.1	0.5	0.1
σ	0.4	0.8	0.3	0.1	0.0

Table A4. Sum, average, max, and standard deviation of portable X-Ray Fluorescence (pXRF) surficial elemental results (units of uncorrected XRF counts) from 14 subsamples of the Twin Lakes sample set. The table is sorted from highest-to-lowest average, and elements outside the ten highest average values are not included. Instrument used is the Bruker S1 TITAN using dual method with MudrockAir specifications. See appendix datasets for complete pXRF dataset.

	Si	Cl	Fe	Al	S
SUM	182.7	47.8	45.4	32.6	31.7
AVG	13.0	3.4	3.2	2.3	2.3
MAX	29.3	28.2	11.1	4.9	6.6
σ	6.9	6.9	3.6	1.5	1.9
	Ca	**K**	**Mg**	**Ti**	**P**
SUM	11.2	9.3	7.9	2.9	1.0
AVG	0.8	0.7	0.6	0.2	0.1
MAX	3.9	1.9	1.5	0.8	0.3
σ	1.3	0.5	0.3	0.3	0.1

REFERENCES

[1] K. C. Benison *et al.*, "Sedimentology of acid saline lakes in southern western Australia: Newly described processes and products of an extreme environment," *Journal of Sedimentary Research*, vol. 77, no. 5, pp. 366–388, May 2007, doi: 10.2110/jsr.2007.038.

[2] B. B. Bowen, K. C. Benison, F. E. Oboh-Ikuenobe, S. Story, and M. R. Mormile, "Active hematite concretion formation in modern acid saline lake sediments, Lake Brown, Western Australia," *Earth and Planetary Science Letters*, vol. 268, no. 1–2, pp. 52–63, Apr. 2008, doi: 10.1016/j.epsl.2007.12.023.

[3] B. B. Bowen, S. Story, F. Oboh-Ikuenobe, and K. C. Benison, "Differences in regolith weathering history at an acid and neutral saline lake on the Archean Yilgarn Craton and implications for acid brine evolution," *Chemical Geology*, vol. 356, pp. 126–140, Oct. 2013, doi: 10.1016/j.chemgeo.2013.08.005.

[4] K. C. Benison, "Life and death around acid-saline lakes," *PALAIOS*, vol. 23, no. 9, pp. 571–573, Sep. 2008, doi: 10.2110/palo.2008.S05.

[5] R. Thorne, R. Anand, and A. Suvorova, "The formation of fluvio-lacustrine ferruginous pisoliths in the extensive palaeochannels of the Yilgarn Craton, Western Australia," *Sedimentary Geology*, vol. 313, pp. 32–44, Nov. 2014, doi: 10.1016/j.sedgeo.2014.08.004.

[6] B. B. Bowen and K. C. Benison, "Geochemical characteristics of naturally acid and alkaline saline lakes in southern Western Australia," *Applied Geochemistry*, vol. 24, no. 2, pp. 268–284, Feb. 2009, doi: 10.1016/j.apgeochem.2008.11.013.

[7] K. C. Benison and B. C. Bowen, "The evolution of end-member continental waters: The origin of acidity in southern Western Australia," *GSAT*, vol. 25, no. 6, pp. 4–10, Jun. 2015, doi: 10.1130/GSATG231A.1.

[8] J. M. McArthur, J. V. Turner, W. B. Lyons, A. O. Osborn, and M. F. Thirlwall, "Hydrochemistry on the yilgarn block, western Australia: Ferrolysis and mineralisation in acidic brines," *Geochimica et Cosmochimica Acta*, vol. 55, no. 5, pp. 1273–1288, May 1991, doi: 10.1016/0016-7037(91)90306-P.

[9] K. C. Benison and B. B. Bowen, "Extreme sulfur-cycling in acid brine lake environments of Western Australia," *Chemical Geology*, vol. 351, pp. 154–167, Aug. 2013, doi: 10.1016/j.chemgeo.2013.05.018.

[10] K. C. Benison, W. K. O'Neill, D. Blain, and J. E. Hallsworth, "Water activities of acid brine lakes approach the limit for life," *Astrobiology*, vol. 21, no. 6, pp. 729–740, Jun. 2021, doi: 10.1089/ast.2020.2334.

[11] H. G. Dill, B. Weber, and R. Botz, "Metalliferous duricrusts ('orecretes') - markers of weathering: A mineralogical and climatic-geomorphological approach to supergene Pb-Zn-Cu-Sb-P mineralization on different parent materials," *njma*, vol. 190, no. 2, pp. 123–195, Apr. 2013, doi: 10.1127/0077-7757/2013/0235.

[12] S. Story, B. B. Bowen, K. C. Benison, and D. G. Schulze, "Authigenic phyllosilicates in modern acid saline lake sediments and implications for Mars," *J. Geophys. Res.*, vol. 115, no. E12, p. E12012, Dec. 2010, doi: 10.1029/2010JE003687.

[13] B. B. Bowen, K. C. Benison, and S. Story, "Early Diagenesis by Modern Acid Brines in Western Australia and Implications for the History of Sedimentary Modification on Mars," in *Sedimentary Geology of Mars*, J. P. Grotzinger, Ed. Tulsa: SEPM (Society for Sedimentary Geology), 2012, pp. 229–252. doi: 10.2110/pec.12.102.

[14] D. Long and W. Lyons, "Aridity, continental evolution, and ground-water chemistry," *GSA Today*, vol. 2, no. 9, pp. 185–190, Sep. 1992.

[15] M. E. Elwood Madden, R. J. Bodnar, and J. D. Rimstidt, "Jarosite as an indicator of water-limited chemical weathering on Mars," *Nature*, vol. 431, no. 7010, pp. 821–823, Oct. 2004, doi: 10.1038/nature02971.

[16] W. H. Farrand, T. D. Glotch, J. W. Rice, J. A. Hurowitz, and G. A. Swayze, "Discovery of jarosite within the Mawrth Vallis region of Mars: Implications for the geologic history of the region," *Icarus*, vol. 204, no. 2, pp. 478–488, Dec. 2009, doi: 10.1016/j.icarus.2009.07.014.

[17] M. E. Elwood Madden, A. S. Madden, and J. D. Rimstidt, "How long was Meridiani Planum wet? Applying a jarosite stopwatch to determine the duration of aqueous diagenesis," *Geology*, vol. 37, no. 7, pp. 635–638, Jul. 2009, doi: 10.1130/G25639A.1.

[18] J. J. Papike, J. M. Karner, and C. K. Shearer, "Comparative planetary mineralogy: Implications of martian and terrestrial jarosite. A crystal chemical perspective," *Geochimica et Cosmochimica Acta*, vol. 70, no. 5, pp. 1309–1321, Mar. 2006, doi: 10.1016/j.gca.2005.11.004.

[19] B. L. Dickson and A. M. Giblin, "Features of acid–saline systems of Southern Australia," *Applied Geochemistry*, vol. 24, no. 2, pp. 297–302, Feb. 2009, doi: 10.1016/j.apgeochem.2008.11.011.

[20] J. L. Bishop, M. D. Lane, M. D. Dyar, and A. J. Brown, "Reflectance and emission spectroscopy study of four groups of phyllosilicates: Smectites, kaolinite-serpentines, chlorites and micas," *Clay miner.*, vol. 43, no. 1, pp. 35–54, Mar. 2008, doi: 10.1180/claymin.2008.043.1.03.

[21] R. N. Clark, T. V. V. King, M. Klejwa, G. A. Swayze, and N. Vergo, "High spectral resolution reflectance spectroscopy of minerals," *JGR Solid Earth*, vol. 95, no. B8, pp. 12653–12680, 1990, doi: 10.1029/JB095iB08p12653.

[22] A. J. Brown, "Spectral curve fitting for automatic hyperspectral data analysis," *IEEE Trans. Geosci. Remote Sensing*, vol. 44, no. 6, pp. 1601–1608, Jun. 2006, doi: 10.1109/TGRS.2006.870435.

[23] R. N. Clark, "Spectroscopy of Rocks and Minerals and Principles of Spectroscopy. Manual of Remote Sensing," in *Manual of Remote Sensing Vol. 3:*, 3rd ed., vol. 3, A. N. Rencz and R. A. Ryerson, Eds. New York: Wiley, 1999, pp. 3–58.

[24] R. N. Clark *et al.*, "USGS digital spectral library splib06a," US Geological Survey, Sep. 2007. [Online]. Available: http://speclab.cr.usgs.gov/spectral.lib06

[25] G. Hunt, "Spectral signatures of particulate minerals in the visible and near infrared," *Geophysics*, vol. 42, no. 3, pp. 501–513, Apr. 1977, doi: 10.1190/1.1440721.

[26] S. Story, "MINERALOGY OF ACID SALINE LAKE SYSTEMS IN SOUTHERN WESTERN AUSTRALIA," Dissertation, Purdue University, Indiana, 2012.

[27] H. N. Cutten, A. Riganti, and J. R. Kirk, "1:100,000 State interpreted bedrock geology of Western Australia," Government of Western Australia, Department of Mines, Industry Regulation and Safety, Western Australia, 2019. [Online]. Available: http:/www.dmp.wa.gov.au/datacentre

[28] T. Cocks, R. Jenssen, A. Stewart, I. Wilson, and T. Shields, "The HyMap Airborne Hyperspectral Sensor: The System, Calibration and Performance," presented at the EARSEL Workshop on Imaging Spectroscopy, Zurich, Switzerland, 1998, p. 6.

[29] P. Virtanen *et al.*, "SciPy 1.0: fundamental algorithms for scientific computing in Python," *Nat Methods*, vol. 17, no. 3, pp. 261–272, Mar. 2020, doi: 10.1038/s41592-019-0686-2.

[30] D. W. Scott, "Kernel Density Estimators," in *Multivariate Density Estimation: Theory, Practice, and Visualization*, 1st ed., Wiley, 2015. doi: 10.1002/9781118575574.

[31] B. W. Silverman, "Density Estimation for Statistics and Data Analysis," *Monographs on Statistics and Applied Probability*, 1986.

[32] R. M. Cornell and U. Schwertmann, *The Iron Oxides: Structure, Properties, Reactions, Occurrence and Uses*. Weinheim, Germany: VCH, 1996.

[33] J. Banfield, "The Mineralogy and Chemistry of Granite Weathering," Australian National University, Canberra, 1985.

[34] J. A. Hurowitz, W. W. Fischer, N. J. Tosca, and R. E. Milliken, "Origin of acidic surface waters and the evolution of atmospheric chemistry on early Mars," *Nature Geosci*, vol. 3, no. 5, pp. 323–326, May 2010, doi: 10.1038/ngeo831.

[35] V. B. Asio and R. Jahn, "Weathering of basaltic rock and clay mineral formation in Leyte, Philippines," *The Philippine Agricultural Scientist*, vol. 90, no. 3, pp. 192–204, 2007.

[36] J. A. Hurowitz *et al.*, "In situ and experimental evidence for acidic weathering of rocks and soils on Mars," *J. Geophys. Res.*, vol. 111, no. E02S19, p. 16, Feb. 2006, doi: 10.1029/2005JE002515.

[37] S. E. Williams, J. M. Whittaker, J. A. Halpin, and R. D. Müller, "Australian-Antarctic breakup and seafloor spreading: Balancing geological and geophysical constraints," *Earth-Science Reviews*, vol. 188, pp. 41–58, Jan. 2019, doi: 10.1016/j.earscirev.2018.10.011.

[38] K. C. Benison and B. B. Bowen, "Acid saline lake systems give clues about past environments and the search for life on Mars," *Icarus*, vol. 183, no. 1, pp. 225–229, Jul. 2006, doi: 10.1016/j.icarus.2006.02.018.

[39] R. G. Burns, "Schwertmannite on Mars: Deposition of This Ferric Oxyhydroxysulfate Mineral in Acidic Saline Meltwaters," pp. 14–18, Mar. 1994.

[40] K. C. Benison and D. A. LaClair, "Modern and Ancient Extremely Acid Saline Deposits: Terrestrial Analogs for Martian Environments?," *Astrobiology*, vol. 3, no. 3, pp. 609–618, Sep. 2003, doi: 10.1089/153110703322610690.

[41] A. J. Brown, M. R. Walter, and T. Cudahy, "Hyperspectral Imaging Spectroscopy of a Mars Analog Environment at the North Pole Dome, Pilbara Craton, Western Australia," *Australian Journal of Earth Sciences*, no. Miscellany, p. 21, Feb. 2007, doi: 10.1080/08120090500134530.

[42] B. C. Clark *et al.*, "Chemistry and mineralogy of outcrops at Meridiani Planum," *Earth and Planetary Science Letters*, vol. 240, no. 1, pp. 73–94, Nov. 2005, doi: 10.1016/j.epsl.2005.09.040.

[43] S. W. Squyres *et al.*, "In Situ Evidence for an Ancient Aqueous Environment at Meridiani Planum, Mars," *Science*, vol. 306, no. 5702, pp. 1709–1714, Dec. 2004, doi: 10.1126/science.1104559.

Mark Radwin (Member, GRSS) is from Boston, MA, USA, born in 1997. B.S. Geoscience, Environmental emphasis, University of Utah, Salt Lake City, UT, USA, 2020. M.S. Geology, University of Utah, Salt Lake City, UT, USA, 2022. He has worked as a NASA DEVELOP participant during the summer of 2021 and is currently a Ph.D. student at the University of Utah.

Brenda B. Bowen is a Professor of Geology and Geophysics and the Director of the Global Change and Sustainability Center at the University of Utah. B.S. 1998 and M.S. 2000 in Earth Sciences, University of California, Santa Cruz. Ph.D., Geology, University of Utah, Salt Lake City, UT 2005.

Kathleen Benison is a Professor of Geology at West Virginia University. She is a participating scientist on the Mars 2020 mission and a science editor for the journal *GEOLOGY*. B.S. 1990 in Geology and Chemistry, Bridgewater State College, Bridgewater, MA. M.A. 1993 in Geology, Binghamton University, Binghamton, NY. Ph.D. 1997 in Geology, University of Kansas, Lawrence, KS, 1997.

Stacy Story is a Petrophysicist at ExxonMobil. B.S. 2004, Biological Sciences, University of Missouri - Rolla. B.S. and M.S. 2006, Geology and Geophysics, University of Missouri - Rolla. Ph.D. 2012, Earth and Atmospheric Sciences, Purdue University.